

Laterally decorated ribbon-shaped graphene segments made of twelve benzene units self-assemble into a nematic anisotropic glass at room temperature with high birefringence and polarized fluorescence.

## An unusual plank-shaped nematogen with a graphenenanoribbon core

Giliandro Farias,<sup>a</sup> David S. Simeão,<sup>b</sup> Thamires S. Moreira,<sup>c</sup> Paloma L. dos Santos,<sup>d</sup> Ahmed Bentaleb,<sup>c</sup> Edivandro Giroto,<sup>a</sup> Andrew P. Monkman,<sup>d</sup> Juliana Eccher,<sup>e</sup> Fabien Durolo,<sup>c</sup> Harald Bock,<sup>\*c</sup> Bernardo de Souza,<sup>\*a</sup> and Ivan H. Bechtold<sup>\*e</sup>

<sup>a</sup> Departamento de Química, Universidade Federal de Santa Catarina 88040-900 Florianópolis, SC, Brazil; bernardo.souza@ufsc.br.

<sup>b</sup> Departamento Acadêmico de Física, Universidade Tecnológica Federal do Paraná, 86036-370 Londrina, PR, Brazil.

<sup>c</sup> Centre de Recherche Paul Pascal, CNRS & Université de Bordeaux, 115, av. Schweitzer, 33600 Pessac, France; bock@crpp-bordeaux.cnrs.fr.

<sup>d</sup> Department of Physics, Durham University, South Road, Durham, DH1 3LE, U.K.

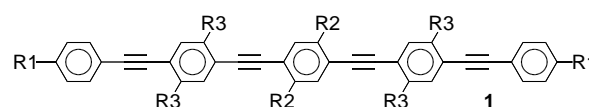
<sup>e</sup> Departamento de Física, Universidade Federal de Santa Catarina, 88040-900 Florianópolis, SC, Brazil; ivan.bechtold@ufsc.br.

The authors are grateful to CNPq, CAPES, FAPESC, INCT-INEO, H2020-MSCA-RISE-2017 (OCTA, #778158) and CAPES-COFEUCUB (Ph-C 803-14) for financial support.

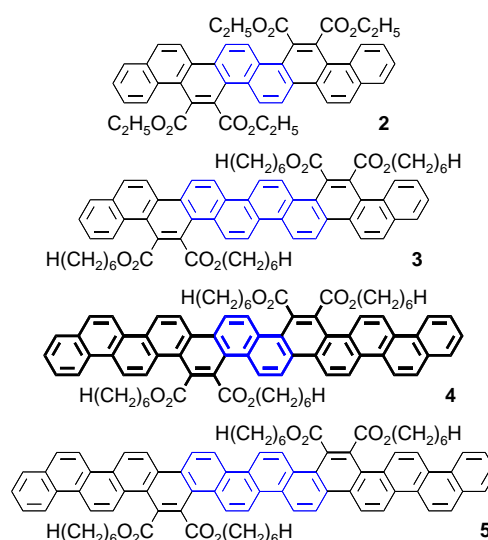
**A [12]phenacene exclusively decorated with four lateral hexylester substituents self-assembles into a nematic liquid crystal glass on cooling after melting at high temperature. This uniaxial nematic organization of a plank-shaped nanographene is unprecedented and in strong contrast to the common design rules for liquid crystals. Highly birefringent samples emitting polarized fluorescence can be obtained in homogeneously planar or twisted waveguiding configurations that are stable against crystallization at and below room temperature and up to 100°C.**

Nematics are the simplest and most abundant type of liquid crystals, and come in a great variety of molecular structures. To form a standard (uniaxial) nematic mesophase, i.e. a liquid with no long-range positional molecular order but with macroscopic anisotropic orientation along one preferred direction, one of two basic molecular shapes is generally required: Either the semi-flexible molecule is long in one dimension and short in the two others, i.e. a semi-flexible rod, or it is long in two dimensions and short in the third, i.e. a semi-flexible disk. Whilst rod-shaped nematogens are extremely abundant, disk-shaped ones are much rarer, because bidimensional disk-shaped molecules tend to aggregate more strongly than rods and thus prefer columnar mesophases with periodic positional order. The most common molecular structure of rod-shaped nematogens is a combination of two or more benzene units, linked either directly as in biphenyl, or via linker moieties such as  $-\text{COO}-$  or  $-\text{N}=\text{CH}-$ , plus one or two terminal flexible linear alkyl, alkoxy or alkylester substituents, that lengthen further the structure and add flexibility. Often also a polar head group, such as  $-\text{CN}$ , is present, increasing the polarizability of the conjugated pi-electron system along the rod. The flexible alkyl substituents are almost always linked to the head or tail of the aromatic rod-shaped unit, and not laterally, because lateral substitution reduces the anisotropic molecular shape and quickly leads to the loss of the nematic behavior. Even if the aromatic part is extremely elongated, only very small lateral alkyl extensions are tolerated, and terminal alkyl groups should preferably be present as well to compensate the lateral extension. A particularly illustrating example is the family of terminally and laterally alkyl-substituted 1,4-bis[2-[4-(2-phenylethynyl)phenyl]ethynyl]-benzenes **1** described by Yatabe et al.<sup>1</sup> The alkyl substituents R1, R2 and R3 on its near-ideally rod-shaped, strongly nematogenic core have been varied systematically to study the destabilization of the nematic behavior by lateral alkyl substitution and its stabilization by terminal alkyl substitution. With R1=octyl, R2=hexyl and R3=H, i.e. with two long terminal and two long lateral chains, an enantiotropic nematic phase was observed, but if R3 is

increased to ethyl, no mesophase was observed. The mesophase reappears if R2 is shortened to ethyl (i.e. with R1=octyl and R2=R3=ethyl), but even without R2, lengthening R3 just to propyl destroys the mesophase in spite of the presence of long terminal chains R1. With R1=R3=H and R2=octyl, i.e. with only two long lateral chains, no mesophase was observed either. Thus even in this family that has an extremely pronounced rod shape of the rigid part of the molecule, the nematic mesophase is very fragile towards the introduction of lateral alkyl chains.



**Scheme 1.** Near-ideally rod-shaped phenylethynyl tetramers, whose nematic mesophase is easily suppressed by introducing lateral alkyl chains R2 and R3.<sup>1</sup>



**Scheme 2.** Plank-shaped phenacenes with four lateral alkylester chains.<sup>5</sup> Central unsubstituted phenacene fragments are marked in blue. The nematic liquid crystalline homologue **4** is highlighted in bold.

If the conjugated rigid part of the molecule is itself extended in one lateral direction, one would expect increased stacking, favoring 3D crystalline, 2D columnar or 1D smectic (lamellar) periodicity at the expense of nematic (i.e. orientation-only) order. This strong tendency to stack via intermolecular dipolar or pi-electron interactions also has thwarted efforts to obtain

the elusive biaxial nematic mesophase with rigid plank-shaped mesogens; this goal has instead been reached by less rigid lateral extensions using flexible macrocycles<sup>2</sup> or bow-shaped mesogens.<sup>3</sup> Extended semi-flexible molecular cores bearing more than two terminal chains (the so-called tetra- and hexacatenarmesogens) have also failed to give a biaxial nematic mesophase, but they give in some cases a standard (uniaxial) nematic mesophase.<sup>4</sup>

Some of us recently developed the synthesis of long phenacenes decorated with four solubilizing lateral alkylester moieties,<sup>5</sup> because phenacenes are the simplest fully condensed stable graphene ribbons (in contrast to the much less stable acenes) and thus are of fundamental interest as archetypal pi electron systems. All members of this family, i.e. tetraester derivatives **2-5** of [8]-, [10]-, [12]- and [14]phenacene, directly melt upon heating from the crystalline to the isotropic liquid state, without intermittent appearance of an enantiotropic liquid crystalline mesophase.

We have now found that the [12]phenacene derivative **4** surprisingly shows a monotropic nematic phase when, after melting at 247°C,<sup>6</sup> the isotropic liquid is cooled to 241°C. No nematic behavior could be observed with the shorter and longer homologues **2**, **3** and **5**.

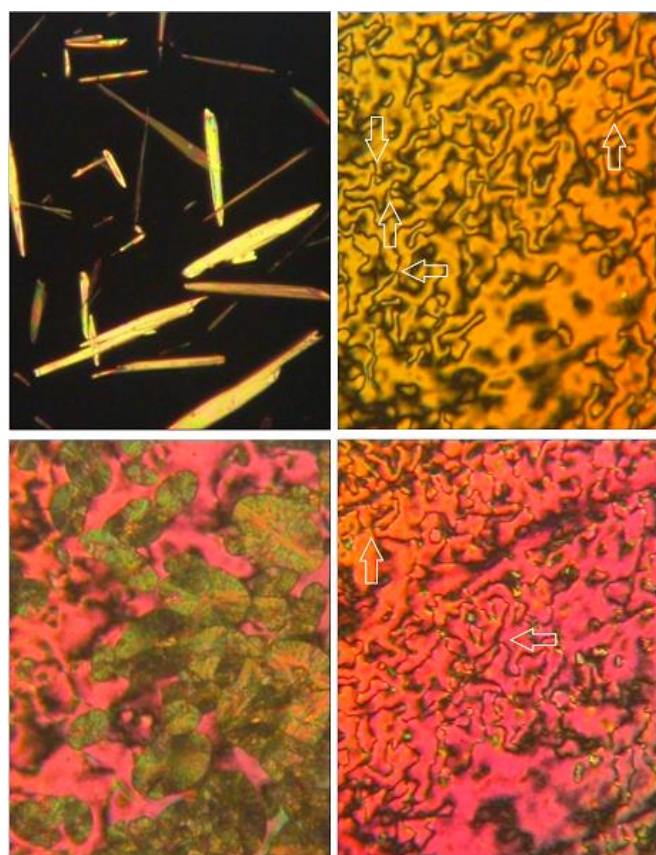


**Figure 1.** Microscopic textures of **4** between untreated glass plates (POM with crossed polarizers): Top left: Melting needle-shaped crystals at 247°C. Top right: Nematic Schlieren texture at 240°C showing four-brush defects (highlighted by arrows) characteristic of a nematic phase of uniaxial symmetry.<sup>7</sup> Bottom left: Nematic texture with spherulitic crystals growing in the bulk upon waiting at 160°C. Bottom right: Nematic Schlieren texture after fast cooling to room temperature, showing four-brush defects (highlighted by arrows).

Given that nematic phases of rod-shaped molecules with only lateral flexible substituents have to our knowledge never been observed before, the occurrence of such a phase in elongated plank-shaped **4** is intriguing, especially in the absence of any such phase in the more elongated **5**. Whilst the absence of a mesophase in the shortest homologue **2** may be attributed to its less anisotropic shape, one possible explanation for the absence of a mesophase in **5** and **3** is that contrary to **4**, both

possess a rather long unsubstituted chrysene fragment in the middle, which allows easier intermolecular non-parallel stacking interactions than the shorter central naphthalene unit in **4**.

Upon slow cooling or when maintaining the sample at a temperature between 100°C and 220°C, crystallization is observed (various crystalline textures can be observed depending on the process). At temperatures above 170°C, this crystal growth nucleates slowly at the rim of the sample, i.e. at defects at its air interface, whilst below 170°C, crystallization starts from multiple nucleation sites in the bulk of the material. Upon fast cooling to temperatures around 100°C or below, the typical nematic Schlieren texture of **4** between glass plates is maintained down to ambient temperature (Figure 1). This suggests that a nematic glass is formed upon fast cooling below a critical temperature, allowing the conservation of nematic order at room temperature. To confirm this, we performed powder X-ray diffraction studies on a bulk sample in a glass capillary at different temperatures (Figure 2). Upon stepwise heating, with diffractograms recorded every 50 degrees, of a sample quickly cooled from 250 to 0°C, only a very broad peak at  $q = 0.35 \text{ \AA}^{-1}$  corresponding to an average intermolecular distance of  $c. 18 \text{ \AA}$  is observed at 0, 50 and 100°C, indicating the absence of any long-range periodicity, whereas crystalline order is manifest at 150 and 200°C. At 250°C, again only a diffuse peak at  $q = 0.35 \text{ \AA}^{-1}$  is observed. Upon stepwise cooling from high temperature to 150°C, with diffractograms recorded every 10 degrees, only the diffuse peak is observed down to 170°C, whilst a multitude of peaks characteristic of crystalline order appear at lower temperature. The lone broad peak corresponding to a distance of  $c. 18 \text{ \AA}$  does not shift significantly at the isotropic-to-nematic transition and only a very slight contraction is observed on fast cooling to room temperature. Albeit no significant difference can thus be discerned between the diffractograms in the isotropic phase at 250°C and those either at lower temperature in the nematic mesophase before the onset of crystallization or at 0 to 100°C in the nematic glass after fast cooling, the absence of any sharp peaks together with the corresponding textures observed by POM confirm conclusively the formation of a nematic phase upon cooling the isotropic liquid and the conservation of the nematic order at low temperature without any “texture-neutral” crystallization that might pass unobserved at POM.

The nematic-to isotropic phase transition manifests itself clearly by differential scanning calorimetry (DSC) as a low-enthalpy transition (0.2 J/g) that shows no significant temperature hysteresis between cooling and heating, whereas the transition to the crystalline state has a hundred times higher transition enthalpy (Figure 3).

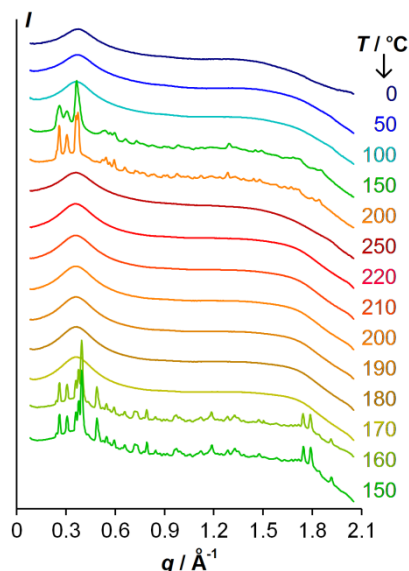


Figure 2. Evolution of the powder X-ray diffraction pattern of a bulk sample of **4** after fast cooling from 250 to 0°C. The sample is first reheated stepwise to 250°C and then cooled stepwise to 150°C (in chronological order from top to bottom, data acquisition time at each temperature: 1 h).

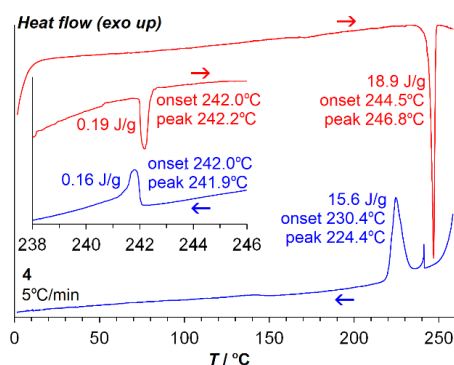


Figure 3. DSC traces for **4** on cooling from the isotropic liquid (blue) and subsequent reheating (red), with transition enthalpies and temperatures. The inset shows the nematic-isotropic transition with reheating after cooling only to just below the transition to avoid crystallization prior to reheating.

As the molecular shape of **4** is moderately biaxial, due both to the flat ribbon shape of the arene core and to the presence of four lateral chains, and as the occurrence of a nematic phase in a lateral-chains-only rod or plank is unprecedented, the question arises whether the nematic mesophase is biaxial. Contrary to Schlieren textures of uniaxial nematics, that display both four- and two-brush defects, four-brush defects are symmetry-impeded in biaxial phases.<sup>7</sup> Albeit the number of four-brush defects is lower in the nematic glass at room temperature than in the fluid mesophase at high temperatures, four-brush defects are clearly present in both (Figure 1); the mesophase is thus uniaxial at all temperatures. The highly delocalized pi electron system suggests a high birefringence  $\Delta n$ , even in the absence of polarizing terminal groups such as cyano (-CN) or isothiocyanato (-NCS), commonly employed in small molecule nematic liquid crystals. Indeed, upon cooling a  $4\mu\text{m} \pm 0.5\mu\text{m}$  thick cell from 250°C down to the onset of crystallization, the birefringence color runs through three color cycles to reach the pale green-yellow beyond third-order red before crystallizing at 170°C, corresponding to a birefringence of  $\Delta n = 0.45 \pm 0.1$ ,<sup>8</sup> a value typically obtained with nematic isothiocyanate mixtures optimized for high birefringence applications.<sup>9</sup> The extended and rigid, yet apolar conjugated pi electron system of **4** thus gives rise to a birefringence that reaches the values of highly polar materials designed for maximum birefringence.

To explore whether the direction of polarization can be homogeneously and macroscopically orientated, we needed an aligning anisotropic surface that is stable and maintains its anisotropy and aligning effect at temperatures close to 250°C, in the vicinity of the phase transition temperatures of **4** where annealing is most efficient. Particularly temperature-resistant aligning surfaces are known to result from rubbing teflon onto heated glass substrates.<sup>10,11</sup> We confirmed that teflon-coated glass plates obtained by rubbing a teflon bar on glass substrates heated to 150°C maintain their microgroove surface structure upon annealing at 260°C (see supporting information). Compound **4** was sandwiched between two teflon-coated glass plates with parallel rubbing directions. After heating the sample to the isotropic liquid at 250°C and then cooling into the nematic phase at 240°C, a homogeneous planar texture was obtained. This uniform alignment could be preserved on fast cooling to room temperature, yielding uniformly oriented birefringent glassy nematic films, whereas slow cooling led to spherulitic crystallization (Figure 4-top). A perfect 90° twisted glassy nematic waveguiding film could be produced with similar ease when a sample between teflon-coated glass plates with perpendicular rubbing directions was cooled quickly from 250°C to room temperature (Figure 4-bottom). These films confirm that the homogeneous director orientation of highly birefringent **4** can be frozen in unidirectional or helical geometries in its nematic glass state.

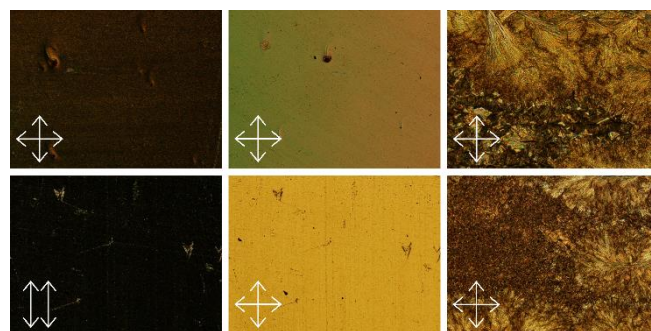
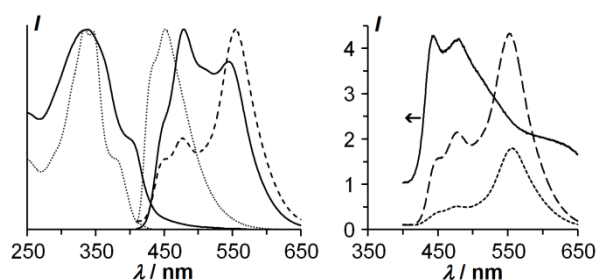


Figure 4. Microscopic textures of **4** between teflon-coated surfaces (POM) after fast (left and center) or slow (right) cooling from 250°C to room temperature. The arrows indicate polarizer and analyzer orientations. Top: uniformly aligned cell; rubbing direction parallel to one polarizer (left) and rubbing direction oblique to both polarizers (center and right). Bottom: 90° twist cell with rubbing directions perpendicular to each other, between parallel (left) and crossed polarizers (center and right).

To assess the effect of homogeneous anisotropic orientation on the fluorescence emission, we compared the emission from solution, from a spin-coated solid film and from the homogeneously teflon-aligned nematic glass (Figure 5). Whereas the absorption maxima in solution (334 and 347 nm) and in the spin-coated film (337 nm) are very similar, the emission shifts from a dominant peak in solution at 451 nm to a much broader two-peaked emission spectrum in the solid (479 and 544 nm in the spin-coated film, 475 and 550 nm in the nematic glass). The absorption of the nematic glass is identical to the spin-coated film. The absorption and emission broadening in the solid and the nematic glass compared to the solution, together with the red shift of the emission, testifies to molecular aggregation.<sup>12</sup> The evolution from a unique shorter-wavelength peak in solution via two near-equally intense peaks in the solid film to a pronounced dominance of the longer-wavelength emission in the nematic glass strongly suggests that intermolecular aggregation with close chromophore contacts and excimer formation is most pronounced in the nematic glassy state with its supposed parallel alignment of chromophores, whilst being less



pronounced in the spin-coated solid film and absent in chloroform solution.



**Figure 5.** Left: Normalized absorption and emission spectra of **4** in chloroform solution (dotted) and spin-coated solid film (continuous), and emission in planar Teflon-aligned nematic glass (dashed). Emission spectra upon excitation at 347 nm (solution) or 335 nm (solid film and nematic glass). Right: Polarized emission spectra (arbitrary units) of planar aligned glassy nematic sample parallel (long dashes) and perpendicular (short dashes) to the alignment direction, and their dichroic ratio (continuous).

The absorption and emission in solution as a function of concentration were measured to investigate the origin of the dominant peak around 550 nm for the nematic glass (Figure S2 in supporting information). The appearance of a new absorption shoulder around 425 nm for concentrations higher than  $5 \times 10^{-3} \text{ mol L}^{-1}$  demonstrates that ground state dimers are formed. For concentrations close to  $10^{-2} \text{ mol L}^{-1}$  the peak around 550 nm is already visible, becoming dominant for concentrations close to  $10^{-1} \text{ mol L}^{-1}$ , and the shorter-wavelength peak at 475 nm is red-shifted compared to more dilute solutions. The appearance of a new fluorescence band without vibronic structure at much higher wavelength than the monomeric band observed in dilute solution and its increase with concentration agree with a dimeric origin.

The lifetime  $\tau$  of the excited state of **4** was measured on the planar aligned nematic glass to probe the emitting species separately at 475 nm and 550 nm. The fluorescence decay curves could be satisfactorily fitted only with bi-exponentials, with the main (>90% contribution) component having a lifetime  $\tau_1$  of 1.3 ns at 475 nm and of 3.6 ns at 550 nm, which indicates

different emitting species (Table 1, Figure S3). Excimer formation is in most cases driven by the non-covalent interaction between excited  $\pi$ - $\pi$  stacked molecules, and emission lifetimes of excimers are usually longer than those of monomeric states.<sup>13,14</sup> We thus conclude that the fluorescence of the nematic glass has a contribution of monomeric states at 475 nm and of aggregate states (dimer and excimer) centered at 550 nm.

Surprisingly, the emission from the planar aligned nematic glass is much more strongly polarized at shorter than at longer wavelengths, with the dichroic ratio (between emission polarized parallel and perpendicular to the alignment direction) being 4.2:1 at 475 nm, and dropping to about 2.4:1 at the long-wavelength peak at 550 nm. The lateral aggregation manifested by the longer-wavelength peak leads to a less uniaxial character of the excited (emitting) state compared to the emission from strongly elongated and uniformly aligned individual chromophores at shorter wavelength.

The theoretical modelling of the isolated molecules **2-5** and its dimers yields the same pattern for the observed photophysical properties. By using TD-DFT, we computed the anisotropy of the transition dipole moment from the ground to the first excited state, which is related to the emission spectra and the birefringence. The predicted vertical energy difference between  $S_0$  and  $S_1$  for the isolated molecules and for their dimeric aggregates are coherent with what was observed, with the aggregates having smaller energy differences (Table S1).

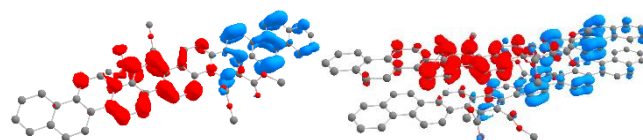
The anisotropy of the transition dipole moment, here measured as the ratio of its  $z$  and  $y$  components (along the ribbon axis and perpendicular to the aromatic plane, respectively), accordingly is much higher for the monomers than for the dimers, and has a strong polarization on the  $z$  axis along the aromatic scaffold (Figure S4 has a full definition of the axes). This is consistent with the observed large birefringence and dichroic ratio.

Figure 6 shows the difference in densities between the  $S_0$  and  $S_1$  states of **4**, with the long chains substituted by a methyl, and its dimer (see Figures S5 and S6 for all molecules). During the electronic excitation (or deexcitation in fluorescence), there is a large electron density shift along the  $z$  axis for the monomer. That is somewhat reduced in the dimer, because parts of the density go along the  $y$  direction, perpendicular to the aromatic rings and into the neighboring molecule. That diminishes the magnitude of the transition dipole vector and correlates directly with the lower emission rate and longer lifetime observed.<sup>15,16</sup>

It appears thus that from the properties of the isolated molecules alone, a reason for **4** being the only material presenting a mesophase cannot satisfactorily be inferred. Whilst the simulations of **2**, with a more isotropic pattern of electron density shifts upon excitation (at least to the  $S_1$ ), may explain its disproportionately low polarizability compared to **3-5**, the electric properties (dipole moment, quadrupole moment and polarizability) of these three longer homologs grow as expected with length and start to saturate at some point, without anything specific to **4** (Figures S7-S9 and Tables S2-S4). This suggests that the propensity to mesophase formation is attributable to a complex combination of short- and medium-range intermolecular interactions in the bulk.

**Table 1.** Excited state lifetimes ( $\tau$ ) obtained from bi-exponential fittings of the fluorescence decay curves, their relative amplitudes ( $A$ ), and fitting factors ( $\chi^2$ ) upon excitation at 475 and 550 nm.

$\lambda / \text{nm}$	$\tau_1 / \text{ns}$	$A_1 / \%$	$\tau_2 / \text{ns}$	$A_2 / \%$	$\chi^2$
475	$1.3 \pm 0.1$	95	$6.0 \pm 0.1$	5	0.998
550	$3.6 \pm 0.2$	92	$11.3 \pm 0.2$	8	0.999



**Figure 6.** Difference in electronic density between the  $S_0$  and  $S_1$  states for a model of molecule **4** and its dimer, calculated using BP86/DEF2-TZVP. The blue represents a depletion while the red an increase in electronic density. Hydrogens are omitted for clarity.

## Conclusions

In summary, extended twelve-ring graphenenanoribbon segments that are appropriately decorated with solubilizing lateral chains self-assemble in parallel to form a strongly anisotropic nematic glass. This amplification of molecular anisotropy into an orientable bulk fluid anisotropic structure, whilst being a trivial feature of liquid crystals, is highly unexpected for graphenenanoribbon segments given their strong tendency to aggregate in positionally ordered  $\pi$ -stacked structures. Uniform macroscopic anisotropic alignment is conveniently obtained in twisted and straight configurations at ambient temperatures, showing high birefringence as well as polarized fluorescence as manifestations of strong anisotropic polarizability, a key prerequisite for graphenenanoribbon optoelectronics.

## Notes and References

- 1 T. Yatabe, Y. Suzuki, Y. Kawanishi, *J. Mater. Chem.* **2008**, *18*, 4468-4477.
- 2 J.-F. Li, V. Percec, C. Rosenblatt, O. D. Lavrentovich, *Europhys. Lett.* **1994**, *25*, 199-204.
- 3 a) M. Lehmann, S.-W. Kang, C. Köhn, S. Haseloh, U. Kolb, D. Schollmeyer, Q. B. Wang S. Kumar, *J. Mater. Chem.* **2006**, *16*, 4326-4334; b) M. Lehmann, C. Köhn, J. L. Figueirinhas, G. Feio, C. Cruz, R. Y. Dong, *Chem. Eur. J.* **2010**, *16*, 8275-8279; c) J. Seltmann, K. Müller, S. Klein, M. Lehmann, *Chem. Commun.* **2011**, 47, 6680-6682.
- 4 M. Gharbia, A. Gharbi, H. T. Nguyen, J. Malthête, *Curr. Opin. Colloid Interface Sci.* **2002**, *7*, 312-325.
- 5 T. S. Moreira, M. Ferreira, A. Dall'armellina, R. Cristiano, H. Gallardo, E. A. Hillard, H. Bock, F. Durola, *Eur. J. Org. Chem.* **2017**, 4548-4551.
- 6 The polymeric microcrystalline material, obtained after repeated column chromatography in dichloromethane on silica followed by repeated crystallization from butanol, partially melts at 242°C, as observed by polarized light optical microscopy (POM), to give way to a mixture of slowly growing crystalline needles surrounded by isotropic liquid. These needles melt upon further heating at 247°C.
- 7 S. Chandrasekhar, G. G. Nair, K. Praefcke, D. Singer, *Mol. Cryst. Liq. Cryst.* **1996**, *288*, 7-14.
- 8 F. D. Bloss, *An Introduction to the Methods of Optical Crystallography*, Saunders College Publishing **1961**, ISBN 0-03-010220-0.
- 9 S. Gauza, J. Li, S.-T. Wu, A. Spadto, R. Dabrowski, Y.-N. Tzeng, K.-L. Cheng, *Liq. Cryst.* **2005**, *32*, 1077-1085.
- 10 J. C. Wittmann, P. Smith, *Nature* **1991**, *352*, 414-417.
- 11 I. H. Bechtold, E. A. Oliveira, *Mol. Cryst. Liq. Cryst.* **2005**, *442*, 41-49.
- 12 P. Apostol, J. Eccher, M. E. R. Dotto, C. B. Costa, T. Cazati, E. A. Hillard, H. Bock, I. H. Bechtold, *Phys. Chem. Chem. Phys.*, **2015**, *17*, 32390-32397.
- 13 E. A. Margulies, L. E. Shoer, S. W. Eaton, M. R. Wasielewski, *Phys. Chem. Chem. Phys.* **2014**, *16*, 23735-23742.
- 14 J. Eccher, A. C. B. Almeida, T. Cazati, H. von Seggern, H. Bock, I. H. Bechtold, *J. Luminescence* **2016**, *180*, 31-37.
- 15 N. J. Turro, J. C. Scaiano, V. Ramamurthy, *Modern Molecular Photochemistry of Organic Molecules*, University Science Books, **2010**, ISBN 978-1891389252.
- 16 B. de Souza, F. Neese, R. Izsák, *J. Chem. Phys.* **2018**, *148*, 034104.

## Supporting information

### General

Spin-coated films of 125 nm thickness with a mean surface roughness of less than 2.0 nm were produced by spinning a solution of 10 mg/mL in chloroform at 1500 rpm for 30 s. The thickness and roughness of the spin-coated films were determined with a Nanosurf Flex AFM, operating in tapping mode under ambient conditions with a scanning rate of 1.0 Hz and 512×512 pixels. Excited state lifetimes were measured at room temperature in air with a DeltaFlex TCSPC system from Horiba using LED excitation at 357 nm and emission collection at 475 nm and 550 nm.

### Atomic force microscopy images of the Teflon treated surfaces

The surface micro-grooves are not significantly affected by annealing the film at 260 °C for 30 s.

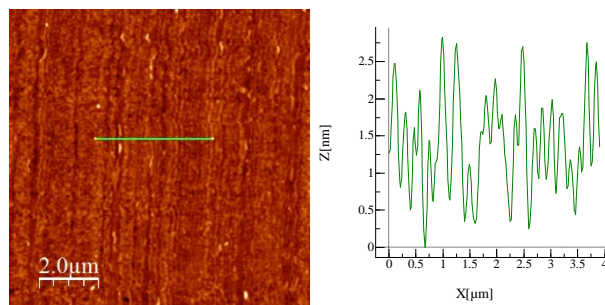
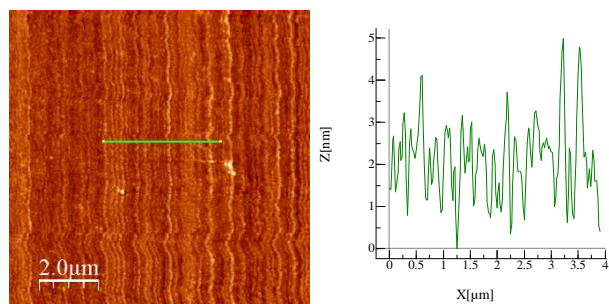


**Figure S1.** AFM images of the Teflon treated surfaces. Top: as rubbed; Bottom: after annealing annealing at 260 °C for 30 s. The left images are cross sections indicated by the green solid line.

### Absorption and emission as a function of concentration

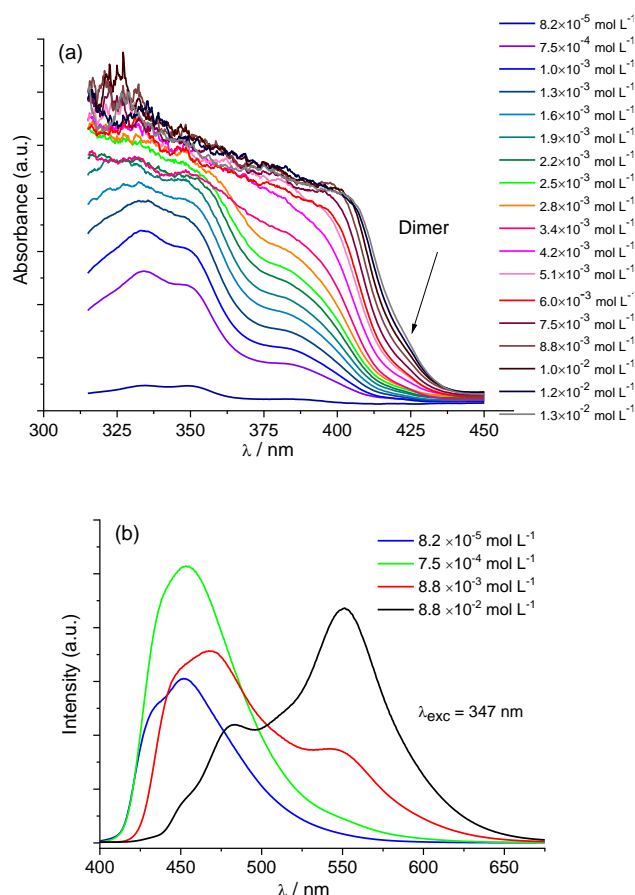


**Figure S2.** (a) Absorption as a function of concentration in chloroform. For concentrations higher than  $5 \times 10^{-3} \text{ mol L}^{-1}$  a shoulder around 425 nm is discernible, which is associated to ground state dimers. (b) Fluorescence spectra at various concentrations:  $8.2 \times 10^{-5} \text{ mol L}^{-1}$  (blue);  $7.5 \times 10^{-4} \text{ mol L}^{-1}$  (green);  $8.8 \times 10^{-3} \text{ mol L}^{-1}$  (red) and  $8.8 \times 10^{-2} \text{ mol L}^{-1}$  (black).

### Excited state lifetime measurement

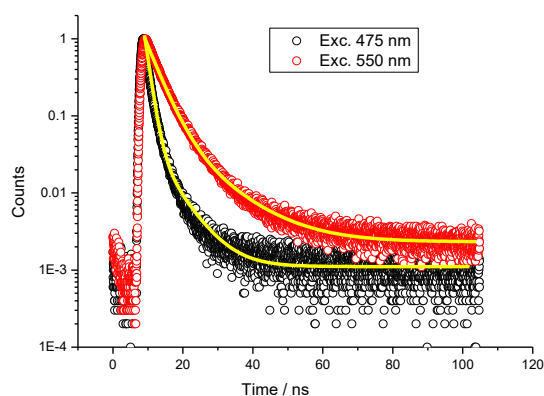


**Figure S3.** Excited state life time in the nematic glass for different excitation wavelengths – black circles: 475 nm; red circles: 550 nm. Yellow solid lines indicate bi-exponential fitting.

## Theoretical Methods

The geometry optimization of **2-5** was carried out in vacuum, using the Orca 4.1<sup>1</sup> software package and DFT with the BP86 functional<sup>2,3</sup> and the DEF2-SVP basis set for all atoms.<sup>4-6</sup> Dispersion effects were included using Grimme's D3 correction with Becke-Johnson (BJ) damping.<sup>7-11</sup> The RIJ algorithm was employed to accelerate the evaluation of the functionals using the resolution of identity approximation for the Coulomb part (RIJ). The vibrational frequencies computed on the optimized geometry of **2-5** included only small negative frequencies (<30 cm<sup>-1</sup>). Their analogues with only methyl moieties instead of longer aliphatic carbon chains (**2C-5C**), or without any ester substituents at all (pure polycyclic arenes, **2A-5A**) and their dimers were also optimized, using the same calculation protocol, but their vibrational frequencies were not verified. All the electric properties were obtained using the same calculation protocol under the expectation value formalism, using a more complete DEF2-TZVP basis for all atoms.<sup>4-6</sup> Time-dependent density functional theory (TD-DFT) under Tamn-Dancoff approximation<sup>12</sup> (TDA) was employed to obtain the first 10 singlet excited states. Images of the complex geometries were obtained using the Chemcraft program.<sup>13</sup>

- [1] F. Neese. *Wiley Interdiscip. Rev. Comput. Mol. Sci.* 2017, 8, e1327.
- [2] Becke, A. D. *Phys. Rev. A* 1986, 38, 3098.
- [3] Perdew, J. P. Yue, W. *Phys. Rev. B* 1986, 40, 3399.
- [4] A. Schäfer, H. Horn, R. Ahlrichs. *J. Phys. Chem.* 1992, 97, 2571.
- [5] A. Schäfer, C. Huber, R. Ahlrichs. *J. Phys. Chem.* 1994, 100, 5829.
- [6] F. Weigend, R. Ahlrichs. *Phys. Chem. Chem. Phys.* 2005, 7, 3297.
- [7] S. Grimme, J. Antony, S. Ehrlich, H. Krieg. *J. Chem. Phys.* 2010, 132, 154104.
- [8] S. Grimme, S. Ehrlich, L. Goerigk. *J. Comput. Chem.* 2011, 32, 1456.
- [9] Becke, A. D. Johnson, E. R. *J. Chem. Phys.* 2005, 122, 154101.
- [10] Johnson, E. R. Becke, A. D. *J. Chem. Phys.* 2005, 123, 024101.
- [11] Johnson, E. R.; Becke, A. D. *J. Chem. Phys.* 2005, 124, 174104.
- [12] T. Petrenko, S. Kossmann, F. Neese, *J. Chem. Phys.* 2011, 134, 054116.
- [13] www.chemcraftprog.com.

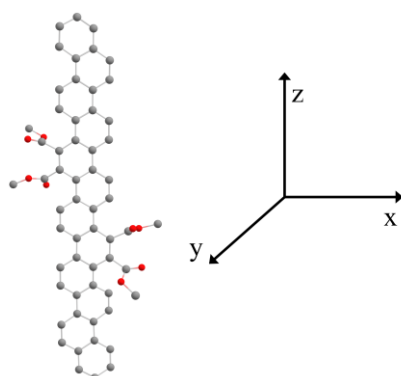
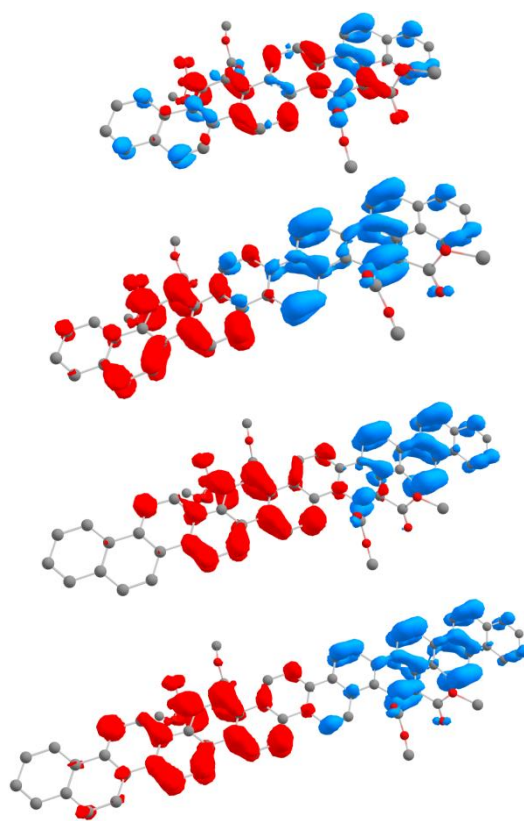


**Figure S4.** Definition of Cartesian axis used in all calculations: the z axis is along the phenylene ribbon and the y axis is perpendicular to the aromatic plane.

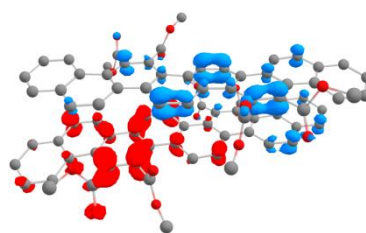
**Table S1.** Data for the TD-DFT vertical excitations using BP86/def2-TZVP on the optimized ground state geometries. The transition dipoles are in atomic units.

Molecule	Theo. / eV <sup>a</sup>	Exp. / eV <sup>b</sup>	$ \langle \mu_x   F \rangle ^2$	$ \langle \mu_y   F \rangle ^2$	$ \langle \mu_z   F \rangle ^2$	$ \mu_x/\mu_y $	
Monomers							
2	2.61	2.61	2.9474	0.1712	-0.0639	1.7070	26.7136
3	2.55		2.1576	0.0419	0.0463	1.4675	31.6954
4	2.46		2.3715	-0.1350	0.0009	1.5340	1704.4444
5	2.42		1.5417	0.1021	0.0539	1.2362	22.9350
Dimers							
2C	2.23	2.25	0.8240	0.1611	-0.1545	-0.8798	5.6945
3C	2.19		0.2240	-0.2405	-0.1611	0.3744	2.3240
4C	2.06		0.0949	-0.1556	-0.0545	0.2602	4.7743
5C	2.06		0.0125	0.0755	-0.0123	-0.0815	6.6260

- a. All of the S<sub>1</sub> states could be described simply from a HOMO-LUMO transition.  
b. From  $\lambda_{\text{max}}$  in solid state.



**Figure S5.** TD-DFT difference densities between ground and first excited states of **2-5** calculated using BP86/def2-TZVP. Hydrogens and aliphatic carbon chains were omitted for clarity. Blue indicates decreased and red indicates increased electronic density.



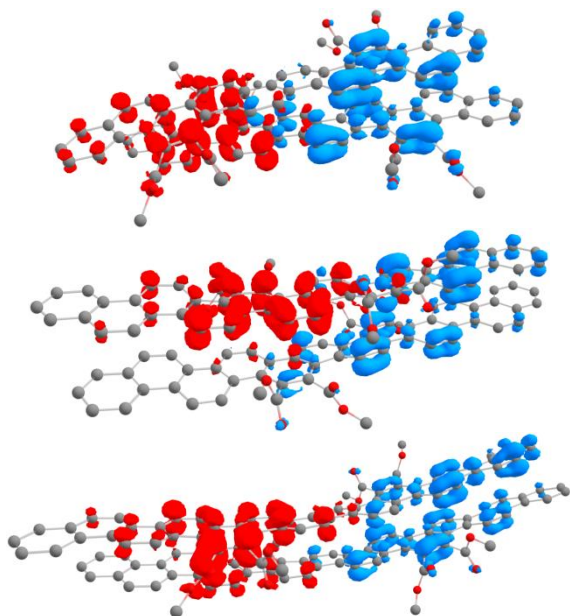


**Figure S6.** TD-DFT difference densities between ground and first excited states of the dimers of **2C-5C** calculated using BP86/def2-TZVP. Hydrogens were omitted for clarity. Blue indicates decreased and red indicates increased electronic density.

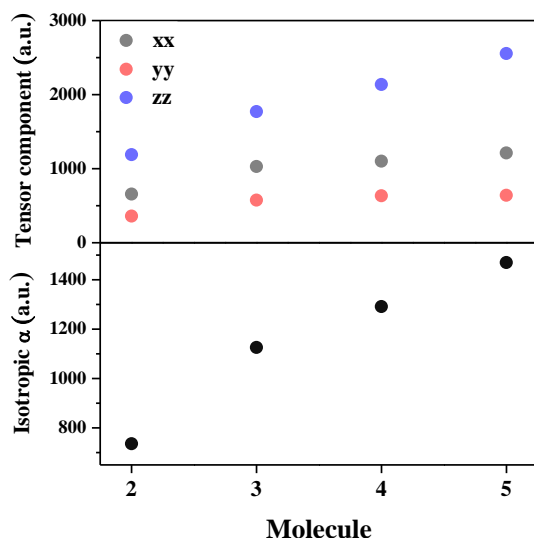


**Figure S7.** Calculated isotropic polarizability and its tensor components (in atomic units) for **2-5** at the BP86/def2-TVZP theory level.

**Table S2.** Calculated isotropic polarizability and its tensor components (in atomic units) for **2-5** and their methyl ester and unsubstituted analogues, at the BP86/def2-TVZP theory level. Compounds **6-7** are similar to **5**, but extending the phenacene ribbon by one (**6**) or two (**7**) benzo (i.e. C<sub>4</sub>H<sub>2</sub>) unit(s) on each end.

Molecule	xx	yy	zz	Isotropic $\alpha$
Complete molecules				
2	656.26	359.42	1189.98	735.22
3	1029.29	576.67	1770.62	1125.52
4	1102.71	633.90	2136.97	1291.19
5	1212.18	639.93	2555.86	1469.32
Methyl ester analogues				
2C	537.94	363.00	1144.87	681.94
3C	668.46	387.72	1496.32	850.83
4C	769.61	386.82	1915.73	1024.05
5C	818.01	452.21	2331.74	1200.65
6C	1051.17	569.73	2496.14	1372.35

7C	1116.09	736.35	2751.34	1534.59
Unsubstitutedarene analogues				
2A	401.79	179.37	1028.37	536.51
3A	480.18	231.78	1393.40	701.79
4A	582.03	259.51	1779.69	873.75
5A	658.21	340.74	2150.19	1049.71
6A	667.69	297.79	2183.43	1049.63
7A	749.78	470.17	2464.68	1228.21

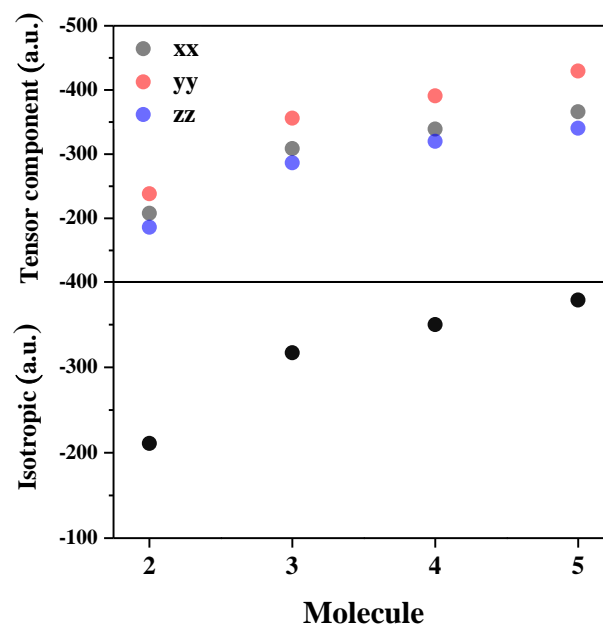


**Figure S8.** Calculated isotropic quadrupole and its tensor components (in atomic units) for **2-5** at the BP86/def2-TVZP theory level.

**Table S3.** Calculated isotropic quadrupole and its tensor components (in atomic units) for **2-5** at the BP86/def2-TVZP theory level.

Molecule	xx	yy	zz	Isotropic
2	-207,93596	-238,33819	-186,20976	-210,82797
3	-308,62054	-355,99027	-286,54043	-317,05041
4	-339,10475	-391,11776	-320,10496	-350,10916
5	-366,1853	-429,42377	-340,33269	-378,64726

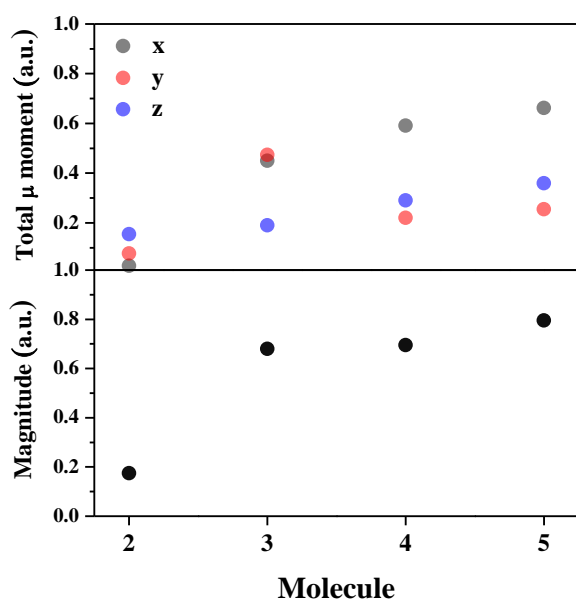


**Figure S9.** Calculated isotropic polarizability and tensor components for **2-5** at the BP86/def2-TVZP theory level.

**Table S4.** Calculated total dipole moment (in atomic units) and its magnitude for **2-5** at BP86/def2-TVZP theory level.

Molecule	$\mu_x$	$\mu_y$	$\mu_z$	Magnitude
<b>2</b>	0.02718	0.07705	0.15424	0.17454
<b>3</b>	0.44996	0.4736	0.18979	0.68028
<b>4</b>	0.59137	0.21987	0.29075	0.69469
<b>5</b>	0.66273	0.25474	0.3593	0.79574

### Differential scanning calorimetry of compound **3**

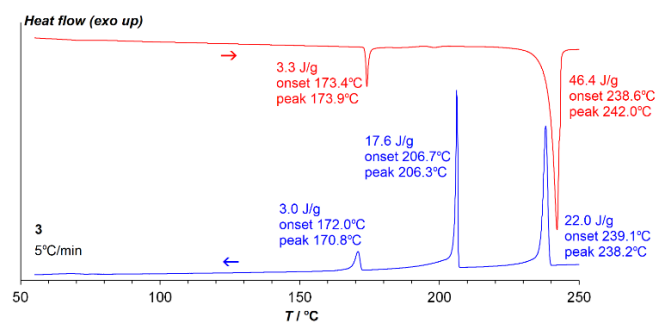


**Figure S10.** DSC traces for homologue **3** (that melts at a similar temperature but contrary to **4** shows no nematic phase) on cooling from the isotropic liquid (blue) and subsequent reheating (red), with transition enthalpies and temperatures.